Postharvest Biology and Technology 49 (2008) 355–365

Contents lists available at ScienceDirect

Postharvest Biology and Technology

journal homepage: www.elsevier.com/locate/postharvbio

Measurement of the optical properties of fruits and vegetables using spatially resolved hyperspectral diffuse reflectance imaging technique

Jianwei Qin[a,1], Renfu Lu[b,*]

[a] Department of Biosystems and Agricultural Engineering, Michigan State University, East Lansing, MI 48824, USA
[b] Sugarbeet and Bean Research Unit, Agricultural Research Service, United States Department of Agriculture, 224 Farrall Hall, Michigan State University, East Lansing, MI 48824, USA

ARTICLE INFO

Article history:
Received 15 June 2007
Accepted 24 March 2008

Keywords:
Hyperspectral imaging
Spatially resolved spectroscopy
Diffuse reflectance
Optical properties
Diffusion theory model
Fruits
Vegetables
Light penetration depth

ABSTRACT

This paper reports on the measurement of the optical properties of fresh fruits and vegetables over the visible and short-wave near-infrared region (500–1000 nm) using a spatially resolved steady-state diffuse reflectance technique. A hyperspectral imaging system in line scan mode was used to acquire spatially resolved diffuse reflectance images from the samples of apple (three varieties), peach, pear, kiwifruit, plum, cucumber, zucchini squash, and tomato (at three ripeness stages) over the spectral range of 500–1000 nm. The absorption and reduced scattering coefficients of the samples were determined from the spatially resolved scattering profiles using inverse algorithms for a diffusion theory model. Spectra of the absorption coefficient were featured by major pigments (chlorophyll, anthocyanin, and carotenoid) and water in the samples, whereas spectra of the reduced scattering coefficient generally decreased with the increase of wavelength. Values of the absorption and reduced scattering coefficients varied greatly among the test samples. Large differences in the absorption spectra were observed for the tomatoes of three ripeness stages (green, pink, and red), and their ripeness was correctly classified using the ratio of the absorption coefficient at 675 nm (for chlorophyll) to that at 535 nm (for anthocyanin). Values of the reduced scattering coefficient positively correlated with the firmness of tomatoes at individual wavelengths of 500–1000 nm, with the maximum correlation of 0.66 being obtained at 790 nm. Light penetration depths, defined as the depths at which the incident light was reduced by 99%, were estimated to be between 0.97 and 6.52 cm for the fruit and vegetable samples over the wavelength range of 500–1000 nm; they were influenced by major pigments in the plant tissue. The spatially resolved steady-state diffuse reflectance technique provides a convenient and efficient means for measuring the optical properties of turbid food and agricultural products.

Published by Elsevier B.V.

1. Introduction

Light interaction with turbid biological materials, such as fruits and vegetables, is a complicated phenomenon involving both absorption and scattering. In a strongly scattering material, photons often undergo multiple scattering before being absorbed or exiting from the material. Light absorption is primarily related to chemical constituents of the material (e.g., sugar), whereas light scattering is influenced by structural/physical characteristics (density, particle size, and cellular structures). These two fundamental optical properties are characterized by the absorption coefficient (μ_a) and reduced scattering coefficient (μ_s') (Tuchin, 2000). Knowledge of these optical properties is critical for quantitative understanding of light interaction with turbid biological materials and the development of effective optical techniques for quality evaluation and safety inspection of food and agricultural products. However, since absorption and scattering are intertwined, they are difficult to measure from intact turbid food and agricultural products using such a technique as near-infrared (NIR) spectroscopy.

Near-infrared spectroscopy is now widely used for determining chemical constituents or quality attributes of food and agricultural products (Williams and Norris, 2001). NIR measurements may be performed from either intact samples or specially prepared samples in reflectance, interactance, or transmittance mode. 'Absorption' spectra are then obtained using the Beer–Lambertian law, which are calculated as the logarithm of the ratio of reflectance or transmittance from the sample to that from a standard. NIR absorption spectra approximately describe the aggregate effect

* Corresponding author.
E-mail addresses: qinj@ufl.edu (J. Qin), renfu.lu@ars.usda.gov, lur@msu.edu (R. Lu).
[1] Current address: Department of Agricultural and Biological Engineering, 233 Frazier Rogers Hall, P.O. Box 110570, University of Florida, Gainesville, FL 32611-0570, USA.

0925-5214/$ – see front matter. Published by Elsevier B.V.
doi:10.1016/j.postharvbio.2008.03.010

of absorption and scattering in food samples; they do not offer separate information on the absorption and scattering properties. Hence, NIR spectroscopy, in essence, is an empirical technique that relies on statistical methods to relate spectral features to the chemical or physical attributes of food samples. Because of its empiricism, conventional NIR measurements are not suitable for quantitative analysis of light absorption and scattering in scattering-dominant food materials.

In contrast to conventional NIR spectroscopy that is widely used for evaluation of food and agricultural products, a different approach has been used in biomedical engineering research to measure or identify different types of biological tissues. This approach is based on the measurement of spectral absorption and scattering properties (i.e., μ_a and μ_s') of turbid materials that may be adequately described by the radiation transfer theory (Roggan et al., 1999; Zonios et al., 1999; Tuchin, 2000; Vo-Dinh, 2003; Zhang et al., 2005; Palmer et al., 2006). This approach would give more information about the sample because absorption and scattering properties are decoupled and obtained simultaneously. Moreover, this fundamental approach provides an important means for analyzing or quantifying light scattering and propagation inside the turbid medium, and hence it could be potentially used for imaging the interior structure of the medium, which would otherwise be impossible with conventional NIR spectroscopy. The approach, however, generally requires more sophisticated instrumentation and complex mathematical algorithms, which could be problematic for food products because of cost and speed concerns. Several methods based on this fundamental approach have been developed for determining μ_a and μ_s' of turbid biological materials. These methods may be divided into three main categories: time-resolved (Patterson et al., 1989), frequency-domain (Patterson et al., 1991), and spatially resolved steady-state methods (Groenhuis et al., 1983b). With the time-resolved and frequency-domain methods, a high-frequency pulse light source and/or a tunable laser source are needed (Fishkin et al., 1997; Ntziachristos and Chance, 2001). The two methods are especially suitable for medical diagnosis of abnormal tissues within a heterogeneous body. However, both time-resolved and frequency-domain methods are expensive in instrumentation and inefficient or time consuming in measurement, and require good contact between the sensor and the object to be measured. In addition, both methods may not cover a wide spectral region due to a limited wavelength tunable range of the light sources currently available (tunable lasers are often required).

The spatially resolved steady-state methods use light sources of constant intensity and multiple detectors at different distances; they are less complicated in instrumentation compared to the time-resolved and frequency-domain methods. Spatially resolved methods can be further divided into contact detection using optical fiber arrays (Nichols et al., 1997; Doornbos et al., 1999; Dam et al., 2001) and noncontact detection based on image reflectometry (Wang and Jacques, 1995; Kienle et al., 1996; Pham et al., 2001). The contact detection method, which has been extensively researched for measuring the optical properties of biological materials, is less desirable for food products because of safety and speed requirements. The noncontact imaging-based method is advantageous for studying food and agricultural products, but it is often limited to single or a few wavelengths.

Techniques for the measurement of optical properties of food and agricultural products are still not well developed, and only limited research has been reported. Cubeddu and colleagues (Cubeddu et al., 2001a,b; Valero et al., 2004) and Chauchard et al. (2005) used time-resolved spectroscopy for determining the optical properties of apples and other fruits. Xia et al. (2007) measured the optical properties of beef muscle for predicting meat tenderness using a spatially resolved technique in contact sensing mode. These techniques are difficult to perform on such food products as fruits and vegetables because of size and geometry limitations, and they are still not viable for assessing, sorting, and grading horticultural products.

Our laboratory has recently developed a hyperspectral imaging-based spatially resolved technique for the measurement of quality attributes of fruit (Lu, 2003, 2007; Lu and Peng, 2006). The technique was further refined and improved for measuring the optical properties of turbid liquid foods (milk and juice) (Qin and Lu, 2007). Compared to time-resolved and spatially resolved techniques in contact sensing mode, the hyperspectral imaging technique is non-contact, faster, and simpler in measuring the optical properties, and hence it would be more suitable for food and agricultural products. This research was aimed to apply this new technique for measuring the optical properties of fruits and vegetables in the visible and short-wave near-infrared region. Specific objectives of this research were to

- develop an improved hyperspectral imaging configuration that is appropriate for measuring spatially resolved reflectance profiles from intact samples of fruits and vegetables,
- derive a mathematical equation for correcting the spatially resolved diffuse reflectance profiles due to the effect of the curved sample surface,
- measure the absorption and reduced scattering coefficients of selected fruit and vegetable samples over the spectral range of 500–1000 nm, and
- demonstrate two examples of using optical properties for estimating the maturity/quality of tomatoes and light penetration depths in the fruit and vegetable samples.

2. Materials and methods

2.1. Diffusion theory model

The radiation transport equation, also known as the Boltzmann equation (Tuchin, 2000), provides a mathematical description for the flow of energy or photons in a scattering system. The original form of the transport equation is rather complicated and difficult to solve either analytically or numerically. However, for a large class of biological materials in which scattering is dominant (i.e., $\mu_s' \gg \mu_a$), the radiation transfer equation can be simplified to a diffusion approximation equation. For certain cases, an analytical solution to the simplified diffusion equation may be obtained. Farrell et al. (1992) studied diffuse reflectance at the surface of a semi-infinite turbid material when it is impinged upon by an infinitely small light source vertically. They derived an analytical solution from the diffusion equation to describe diffuse reflectance, R_f, at the surface of the semi-infinite turbid material as a function of source-detector distance and the optical properties of the investigated material (i.e., the absorption and reduced scattering coefficients, and the relative refractive index), which is given below:

$$R_f(r) = \frac{a'}{4\pi}\left[\frac{1}{\mu_t'}\left(\mu_{eff}+\frac{1}{r_1}\right)\frac{\exp(-\mu_{eff}r_1)}{r_1^2} + \left(\frac{1}{\mu_t'}+\frac{4A}{3\mu_t'}\right)\left(\mu_{eff}+\frac{1}{r_2}\right)\frac{\exp(-\mu_{eff}r_2)}{r_2^2}\right] \quad (1a)$$

where r is the distance from the incident point, a' is the transport albedo [$a' = \mu_s'/(\mu_a + \mu_s')$], μ_{eff} is the effective attenuation coefficient ($\mu_{eff} = [3\mu_a(\mu_a + \mu_s')]^{1/2}$), and μ_t' is the total interaction coefficient ($\mu_t' = \mu_a + \mu_s'$). r_1 and r_2 are expressed by the following

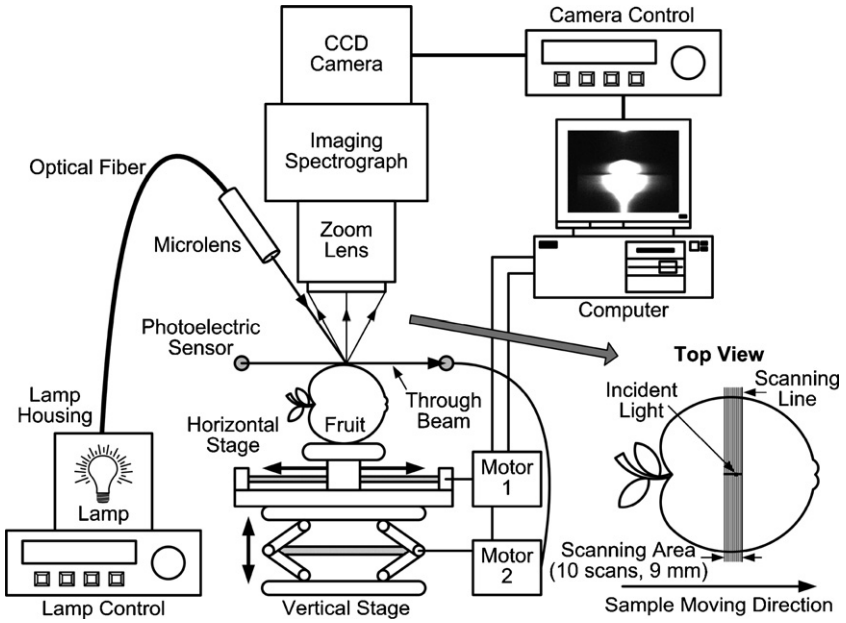

Fig. 1. Hyperspectral imaging system for acquiring spatially resolved scattering images from a fruit sample.

two equations:

$$r_1 = \left[\left(\frac{1}{\mu_t'}\right)^2 + r^2\right]^{1/2} \tag{1b}$$

$$r_2 = \left[\left(\frac{1}{\mu_t'} + \frac{4A}{3\mu_t'}\right)^2 + r^2\right]^{1/2} \tag{1c}$$

where A is an internal reflection coefficient determined by the mismatch of refractive indices at the interface, and it can be calculated from empirical equations (Groenhuis et al., 1983a). In this research, the refractive indices for fruit and vegetable samples were assumed constant (1.35) (Mourant et al., 1997). Once A is determined, the shape of the spatial diffuse reflectance profile is uniquely determined by μ_a and μ_s' through Eq. (1a). Therefore, if the reflectance profile over the surface of the turbid material resulting from a point source is known, μ_a and μ_s' may be determined via Eq. (1a) by an inverse algorithm.

Since scattering is dominant for most biological materials including food and agricultural materials, Farrell model (Eq. (1a)) can satisfactorily describe spatial diffuse reflectance profiles for these materials when they are illuminated with a small size light source. In this research, Farrell model was used for determining the absorption and reduced scattering coefficients of fruits and vegetables. While fruits and vegetables are not exactly semi-infinite homogeneous media, their sizes are generally far greater than the scattering distances (~10 mm) measured. Hence Farrell model could be applied to obtain reasonable results.

2.2. Hyperspectral imaging system

A hyperspectral imaging system (Fig. 1) developed in the U.S. Department of Agriculture Agricultural Research Service (USDA/ARS) postharvest engineering laboratory at Michigan State University in East Lansing, Michigan was used for acquiring spatially resolved scattering images from fruit and vegetable samples. The imaging system mainly consisted of a light source unit, a hyperspectral imaging unit, and a sample handling unit. The light source was a 250-W quartz halogen tungsten lamp with a dc-regulated control housing (Oriel Instruments, Stratford, CT, USA) installed with a digital light intensity controller (Spectra-Physics, Mountain View, CA, USA). The broadband light was coupled to an optic fiber and a microlens to generate a 1.0-mm diameter beam incident upon the sample at 15° from the vertical direction. The optic fiber was 100 μm in diameter and the microlens was 6.4 mm in size and had a focusing distance of ~130 mm. The hyperspectral imaging unit operated in line scanning mode. The unit was composed of a zoom lens, a prism-grating-prism-based imaging spectrograph (ImSpector V10, Spectral Imaging Ltd., Oulu, Finland) covering the spectral range between 400 and 1000 nm, a 512 × 512 pixel back-illuminated CCD camera (Model C4880-21-24A, Hamamatsu Photonics Systems, Bridgewater, NJ, USA) covering the spectral range between 200 and 1100 nm, and a computer equipped with a frame grabbing board for controlling the camera and acquiring images. Reflectance from pixels of the scanned line was dispersed into different wavelengths, which were then projected onto the CCD detector to create a special 2D reflectance image: one dimension represents spatial information and the other dimension spectral. After 2 × 2 binning operations, a hyperspectral scattering image of 256 × 256 pixels was obtained, which had a spectral resolution of 4.54 nm/pixel and a spatial resolution of 0.20 mm/pixel.

Different from the image acquisition method for liquid samples used in the previous study (Qin and Lu, 2007), a new sample handling unit was assembled for automatically positioning each sample for imaging. Two motor-controlled stages were used to control the position and the movement of the sample. A miniature photoelectric sensor (E3T-ST12, Omron Electronics, Schaumburg, IL, USA) served to generate a horizontal through-beam at a predetermined height, and it was used as the benchmark for adjusting the height of the samples. To maintain the same surface height for all samples with different sizes, the vertical stage elevated each sample to the predetermined level of the through-beam. When the sample blocked the light beam, the receiving sensor sent a signal to the motor, and the vertical stage was stopped automatically. Thereafter, the precision stage with a horizontal displacement accuracy of 0.36 μm (MM-4M-EX-80, National Aperture, Salem, NH, USA) carried the sample at a constant speed in the direction perpendicular to the scanning line of the imaging spectrograph (Fig. 1). The movement of both vertical and horizontal stages was controlled

by a computer through the serial ports connected to the motors, and the stage control program was incorporated into the CCD camera control software to synchronize the sample movement and the image acquisition.

The hyperspectral imaging system was calibrated both spectrally and geometrically by following the procedure described by Lu and Chen (1998). Spectral calibrations were performed using spectral calibration lamps (i.e., mercury, xenon, and krypton) and a fluorescence light. Geometrical calibrations were done with a white paper printed with thin parallel lines of 2 mm apart. Moreover, any optical design imperfection and other factors (e.g., specific settings of the lens and prisms) would cause a nonuniform instrument response along the slit of the imaging spectrograph, which would in turn affect the measurement of spatial reflectance profiles. Hence in addition to spectral and geometrical calibrations, a third calibration procedure was performed to correct the nonuniform instrument responses over the wavelengths of 400–1000 nm. The instrument response calibration required a specially assembled calibration device consisting of a light source and a Teflon standard mounted on a platform carried by a high precision motor-controlled stage. Detailed procedures for nonuniform instrumental calibrations for the hyperspectral imaging system can be found in Qin and Lu (2007).

The hyperspectral imaging system line scanned the sample 1.6 mm off the incident point to avoid saturating the CCD detector by high intensity signals near the incident point but without losing essential scattering information. The hyperspectral imaging system collected spatially resolved scattering images from each sample for every 1 mm horizontal displacement over a range of 9 mm (10 scans, see Fig. 1) as it was moving at the pre-determined velocity of 1 mm/s during the image acquisition. Each 2D hyperspectral scattering image was obtained with the camera exposure time of 0.1 s. Compared to the method of single line scanning at a fixed position in the previous study, the new method would provide more accurate measurements of the optical properties of samples since individual scanning images were averaged over the scanning area of the fruit surface, and only average images were used for further analysis.

2.3. Fruit and vegetable samples

Eight samples each of five fruits, including apple ('Golden Delicious', 'Red Delicious' , and 'Fuji'), peach, pear, kiwifruit, and plums, and two vegetables (cucumber and zucchini squash) were purchased at a local supermarket. In addition, 60 tomatoes, 20 for each of the three ripeness stages (green, pink, and red), were also used in the experiment. These tomatoes were harvested from an experimental field at the Michigan State University Horticultural Teaching and Research Center in Holt, MI, USA in August 2006.

The equatorial diameter of each sample was measured using a digital caliper after imaging, which was later used for correcting the hyperspectral scattering profiles. The firmness of tomatoes was measured from the same imaging area after removal of fruit skin, using a texture analyzer (Model TA.XT2i, Stable Micro Systems, Inc., Surrey, UK) equipped with a 3-mm Magness–Taylor (MT) probe at a loading speed of 2 mm/s. Force/displacement curves were recorded for up to a penetration depth of 8 mm and maximum forces were chosen as the reference values of fruit firmness.

2.4. Correction for the size effect of samples

Reflectance measurements for fruits and vegetables are affected by the curvature of each sample. To obtain consistent reflectance signals from the samples, the effect of the fruit surface curvature should be taken into account in the measured reflectance scattering profiles. The effect of the curved fruit surface on reflectance measurements are illustrated in Fig. 2a, in which r_a is the radius of the fruit that is assumed to be circular or cylindrical, r_z is the radius of the zoom lens, L is the object distance, r is the horizontal distance to the illumination center, I_v is the normal component of the reflectance at the fruit surface, and I represents an arbitrary reflectance intensity component entering the imaging system. It was assumed that the reflectance emitted from the sample surface at a given point obeys the Lambertian Cosine Law (Kortüm, 1969), which is valid for turbid materials, as confirmed by Kienle et al. (1996). This means that the component I with an angle θ with respect to the surface normal can be calculated as $I = I_v \cos\theta$.

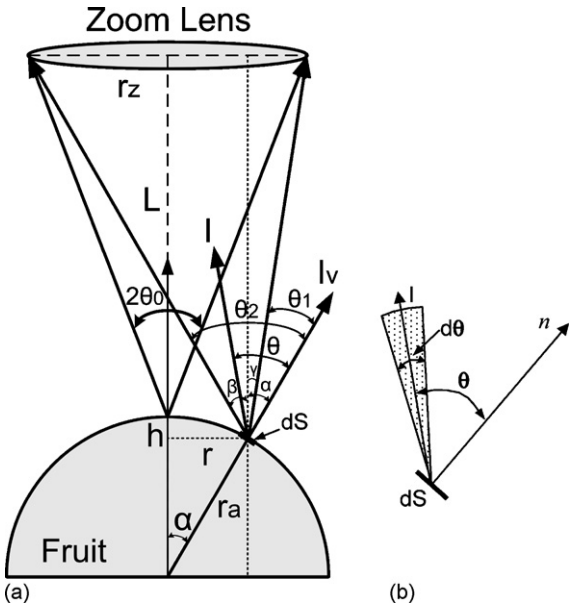

Fig. 2. Correction for light intensity distortion caused by the curved surface of the sample: (a) the geometric relationships between the imaging system and the fruit and (b) the radiance emitting from a line element dS within an angle dθ (the shaded area) at an angle θ to the normal of the line element.

Consider the light energy emitting from a very small line element dS at a distance r from the illumination center. Since the line element dS is very small, it can be approximated to be a straight line. The light power passing through the line element dS inside a shaded area of angle dθ at an angle θ to the normal direction of the line element dS (Fig. 2b) is given by

$$dR = I(dS\cos\theta)d\theta = (I_v\cos\theta)(dS\cos\theta)d\theta \quad (2)$$

where d$S\cos\theta$ represents the projected length of the line element that is perpendicular to the direction of radiation, and the Lambertian cosine law has been applied (i.e., $I = I_v\cos\theta$). The total energy or reflectance, R_e, entering the imaging system from the line element dS is the integration of the reflectance component I over the acceptance angle $(\theta_2 - \theta_1)$ of the zoom lens (Fig. 2a), which can be calculated by the following equation:

$$R_e(r) = \int_{\theta_1}^{\theta_2} I_v\,dS\cos^2\theta\,d\theta = I_v dS\left[\left(\frac{\theta_2}{2} + \frac{\sin 2\theta_2}{4}\right) - \left(\frac{\theta_1}{2} + \frac{\sin 2\theta_1}{4}\right)\right] \quad (3)$$

where $\theta_1 = \alpha - \gamma$, $\theta_2 = \alpha + \beta$, $\alpha = \sin^{-1}(r/r_a)$, $\beta = \tan^{-1}((r_z + r)/(L + h))$, $\gamma = \tan^{-1}((r_z - r)/(L + h))$, and $h = r_a - (r_a^2 - r^2)^{1/2}$ (see Fig. 2 for the description of each symbol).

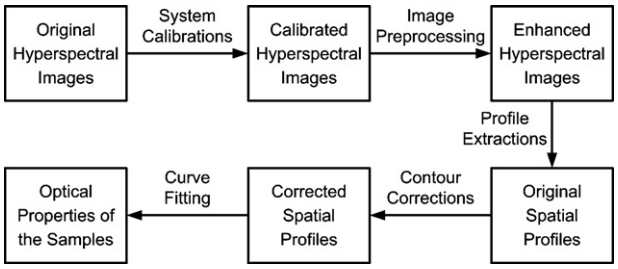

Fig. 3. Procedures for determining the optical properties of fruits and vegetables from the spatially resolved hyperspectral scattering images.

Eq. (3) shows that once the setting of the imaging system (i.e., the distance between the sample and the lens and the lens size) is chosen, the measured reflectance R_e would be dependent on the scattering distance and the curvature of the fruit. The acceptance angle for the measured reflectance at scattering distance $r = 0$ is equal to $2\theta_0$, where $\theta_0 = \tan^{-1}(r_z/L)$. If the scattering distance is greater than zero, the acceptance angle will change, which will in turn affect the measured reflectance. Ideally, the imaging system should collect the reflectance covering the same acceptance angle of $2\theta_0$ at each scattering distance. This cannot be achieved with the current imaging system. However, we may calculate the correct or actual reflectance at any scattering distance based on the knowledge of the normal reflectance component I_v, which is obtained via the following equation:

$$I_v(r) = \left[\left(\frac{\theta_2}{4} + \frac{\sin 2\theta_2}{8}\right) - \left(\frac{\theta_1}{4} + \frac{\sin 2\theta_1}{8}\right)\right]^{-1} \frac{R_e(r)}{dS} \quad (4)$$

The correct reflectance R at scattering distance r should be equivalent to the integration of I over the acceptance angle of $-\theta_0$ to $+\theta_0$ (Fig. 2a), which is given by the following equation:

$$R(r) = \int_{-\theta_0}^{\theta_0} I_v\, dS \cos^2\theta\, d\theta = I_v\, dS \left(\theta_0 + \frac{\sin 2\theta_0}{2}\right) = C(r)R_e(r) \quad (5)$$

where $C(r)$ is the correction factor which is given by

$$C(r) = \frac{\left(\theta_0 + \sin 2\theta_0/2\right)}{(\theta_2/2 + \sin 2\theta_2/4) - (\theta_1/2 + \sin 2\theta_1/4)} \quad (6)$$

Eqs. (5) and (6) were used to correct the measured reflectance profiles for all test samples before the procedure of determining the μ_a and μ_s' values was started.

2.5. Determination of optical properties

Optical properties (μ_a and μ_s') of the fruit and vegetable samples were determined from the spatially resolved hyperspectral images using the steady-state diffusion theory model (Farrell et al., 1992). The data analysis procedures are illustrated in Fig. 3. The original hyperspectral images were first converted to the calibrated images using the information obtained from the spectral, geometrical, and nonuniform instrumental calibrations for the imaging system. Image preprocessing was then performed to improve the signal-to-noise ratio of the calibrated images. Spatially resolved diffuse reflectance profiles were extracted over 500–1000 nm from the enhanced images, followed by the procedure of fruit size corrections for the spatial profiles due to the light intensity distortion caused by the curved fruit surface. This spectral range (500–1000 nm), instead of 400–1000 nm, was chosen because the signals below 500 nm and above 1000 nm were weak and noisy, and thus were not used. Finally, the diffusion theory model was used to fit the corrected experimental data using a trust-region nonlinear least squares fitting algorithm, and the absorption and scattering spectra of the samples were obtained in the spectral region of 500–1000 nm. The above described procedures were implemented in Matlab (The MathWorks, Inc., Natick, MA, USA). A detailed description of the data analysis methods for determining the optical properties using hyperspectral image data can be found in Qin and Lu (2007).

The inverse algorithms described above were validated by testing three types of liquid simulation samples made of intralipid and three absorption solutions (black India ink, blue and green dyes), with accuracies of 16 and 11% for μ_a and μ_s', respectively (Qin and Lu, 2007). It should be noted that an improved version of imaging spectrograph was used in this study, which had less signal distortions and a higher spectral resolution, compared to the one used in the previous study. Hence, the current imaging system would have better accuracies in determining μ_a and μ_s' than the one used in our previous study.

2.6. Estimation of light penetration depths

Knowledge of light penetration depths is valuable because it could help us in designing an appropriate sensing configuration to collect optical information from the interior tissue of a food sample. Different methods of defining or measuring light penetration depths have been reported in literature. Based on the diffusion theory, light penetration depth (δ) may be defined as the traveled distance by which the light intensity level is reduced by a factor of $1/e$ (~37%), and it is computed as the reciprocal of the effective attenuation coefficient (μ_{eff}) (Wilson and Jacques, 1990):

$$\delta = \frac{1}{\mu_{eff}} = \frac{1}{\sqrt{3\mu_a(\mu_a + \mu_s')}} \quad (7)$$

Light intensity in the turbid media follows an exponential decrease with μ_{eff} as the decay constant. Lammertyn et al. (2000) defined the light penetration depth as the fruit slice thickness at which diffuse reflectance spectra were significantly different from those of a slice of infinite thickness. Fraser et al. (2001) suggested the 1% light penetration depth, which is defined as the distance where the light intensity is reduced to 1%. The 1% light penetration depth can be calculated as $\delta \ln(1/1\%) = 4.61\delta$. In this paper, we report on values of the 1% light penetration depth for the fruit and vegetable samples. Since both absorption and scattering properties (μ_a and μ_s') of fruits and vegetables are wavelength-dependent, light penetration depth is also dependent on wavelength. Absorption and reduced scattering spectra of the test samples were used to calculate penetration depths in fruit tissues. For the tomato samples, light penetration depths were calculated only for the mature samples (20 red tomatoes).

3. Results and discussion

3.1. Hyperspectral reflectance images

A typical hyperspectral reflectance image acquired from a Fuji apple is shown in Fig. 4(a), and its 3D display is shown in Fig. 4(b), in which the intensity of the image is illustrated as a third dimension in addition to the spatial and spectral dimensions. The actual spectral range used for determining the optical properties was between 500 and 1000 nm and the effective spatial range was about 20 mm. Each line taken from the image parallel to the spatial axis represents one reflectance profile at a specific wavelength. Three normalized spatial profiles extracted at 600, 675, and 800 nm are shown in Fig. 4(c). The spatial distance for the scattering profiles shown in Fig. 4(c) has been corrected to account for the 1.6 mm distance

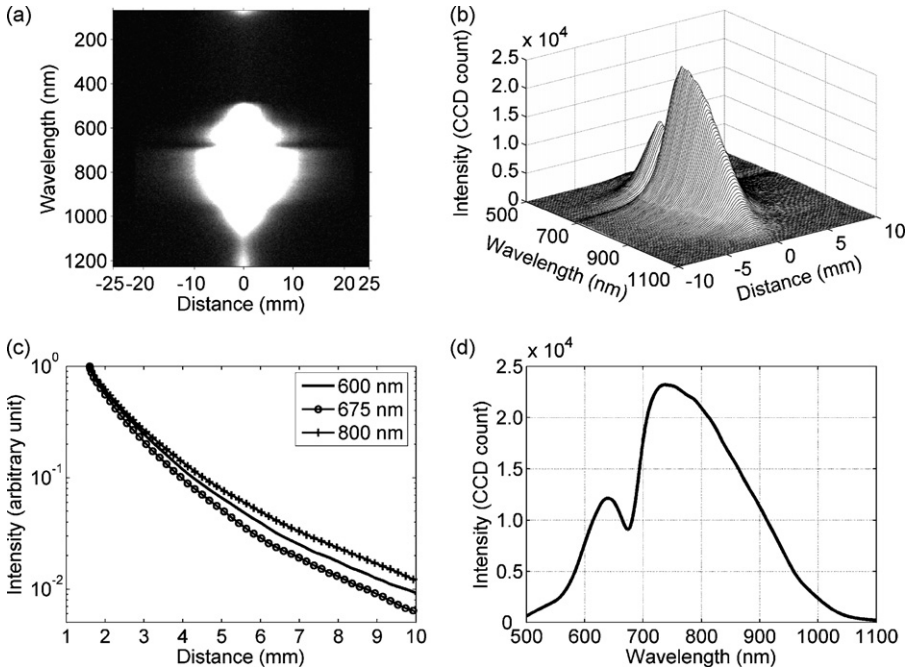

Fig. 4. Hyperspectral scattering image of a Fuji apple: (a) 2D display, (b) 3D display, (c) the normalized spatial profiles at 600, 675, and 800 nm, and (d) a spectrum at 1.6 mm from the light incident point.

between the scanning line and the incident center. The three profiles in Fig. 4(c) are conspicuously different, indicating that the optical properties of the fruit are wavelength-dependent. On the other hand, each line parallel to the spectral axis of the image represents a spectrum at a specific distance. Fig. 4(d) shows a raw spectrum obtained at the nearest spatial point (1.6 mm), in which light absorption by chlorophyll-a in the apple is readily observed around 675 nm.

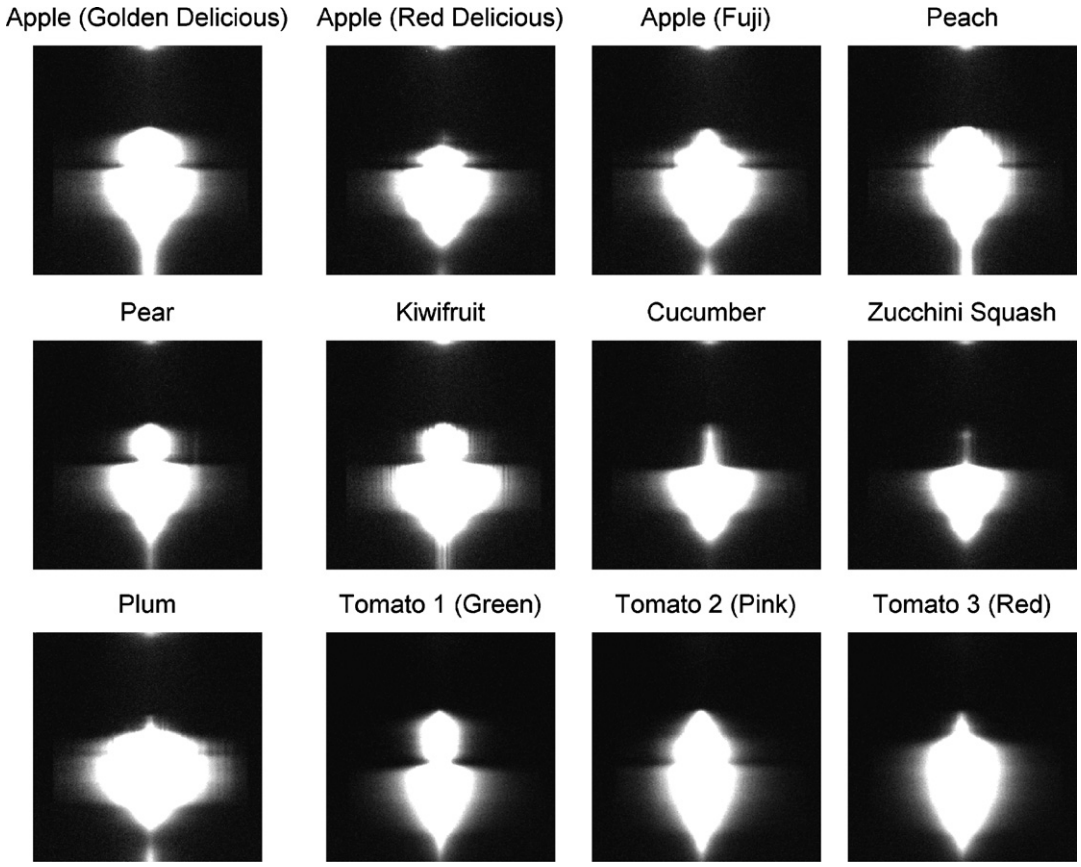

Fig. 5. Original two-dimensional hyperspectral scattering images of selected fruit and vegetable samples. The vertical axis represents the spectral dimension and the horizontal axis represents the spatial dimension.

Fig. 5 shows the original hyperspectral reflectance images from one sample of each fruit and vegetable (including three varieties of apple and three tomatoes with different stages of ripeness (green, pink, and red)). Although the scattering profiles in Fig. 5 cannot be adequately displayed due to the 2D white/black image display format, a quick examination for the pattern of the bright or white area of individual images can reveal some similarities and differences among the samples. A distinct narrowing or bottleneck in the white area of the hyperspectral images at the wavelength of 675 nm was observed for the three varieties of apple (Golden Delicious, Red Delicious, and Fuji), the peach, the pear, the kiwifruit, and the green and pink tomatoes. This narrowing effect was due to light absorption by chlorophyll-a in these fruit and vegetable samples, which in turn reduced the scattering distance. The phenomenon was almost nonexistent in the image of the red tomato because its chlorophyll content would be low or nonexistent. The shapes of the hyperspectral images of the cucumber and the zucchini squash are similar; both had extremely small scattering sizes (due to high levels of absorption) in the visible spectral region. The plum sample was conspicuously different in its scattering image from those of other fruit and vegetable samples; it had a much broader scattering area with no clearly observable chlorophyll absorption effect. This could be due to differences in the pigments and other chemical constituents between the plum and other fruits and/or vegetables.

3.2. Correction factor curves for the test samples

Fig. 6 shows the correction factor (C in Eq. (6)) curves used to correct the spatially resolved scattering profiles of the fruit and vegetable samples, in which the zucchini squash, plum, and Fuji apple were chosen to represent the minimum, medium and maximum sample sizes used in the experiment, respectively. Light intensity distortion caused by the curved fruit surface increased with the spatial distance. At 10 mm from the light incident point, values for the correction factor were 1.28, 1.13, and 1.08 for the zucchini squash, plum and Fuji apple, respectively. This means that the curved fruit surface could cause up to 28% distortion for the intensity of the diffuse reflectance data obtained from the fruit and vegetable samples. Samples with a small diameter (or large curvature) would have larger distortions in the diffuse reflectance signals. The correction factor curves for the zucchini squash and Fuji apple represent the upper and lower bounds for all fruit and vegetable samples used in the experiment, and the correction factor curves for other samples fall between these two curves.

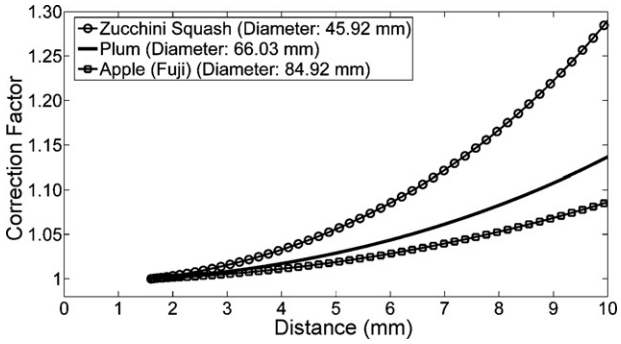

Fig. 6. Correction factor curves calculated using Eq. (6) for correcting the scattering profiles for the three sizes of test samples representing the minimum, medium and maximum sample sizes used in the experiment.

3.3. Optical properties of fruits and vegetables

Typical optical properties over the spectral region from 500 to 1000 nm for nine fruit and vegetable samples are presented in Fig. 7, in which the absorption and reduced scattering spectra of Golden Delicious and Fuji apple, peach, pear, and kiwifruit are shown in Fig. 7(a1) and (a2), respectively, and the absorption and reduced scattering spectra of Red Delicious apple, plum, cucumber, and zucchini squash are shown in Fig. 7(b1) and (b2), respectively. Solid lines in Fig. 7(a2) and (b2) represent the best fits of μ_s' using the following wavelength-dependent function:

$$\mu_s' = a\lambda^{-b} \tag{8}$$

where a and b are parameters for the power series model, and they are related to the density and the average size of the scattering particles, respectively (Mourant et al., 1997; Doornbos et al., 1999). The patterns of μ_a and μ_s' spectra of other samples were generally similar to those shown in Fig. 7, although the absolute values were different due to the variability of individual items within each commodity.

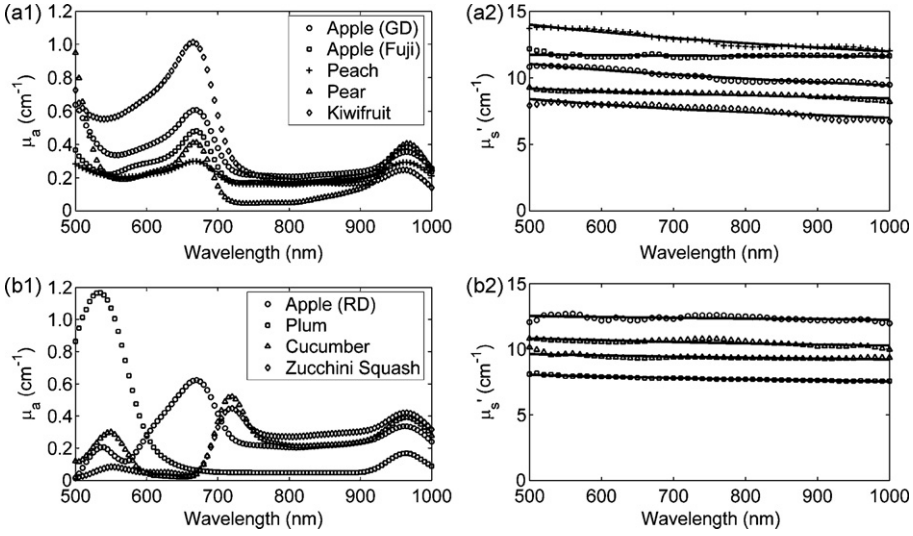

Fig. 7. Optical properties of fruit and vegetable samples: (a1) absorption and (a2) reduced scattering coefficients of Golden Delicious (GD) and Fuji apple, peach, pear, and kiwifruit; (b1) absorption and (b2) reduced scattering coefficients of Red Delicious (RD) apple, plum, cucumber, and zucchini squash. Solid lines in (a2) and (b2) are the best fits of μ_s' using the wavelength-dependent function $\mu_s' = a\lambda^{-b}$, where λ is the wavelength in nm and a and b are constants.

Chemical bonds of biological materials absorb light energy at specific wavelengths (known as 'fingerprints'), thus the absorption properties are wavelength-dependent. The μ_a spectra of the three varieties of apple (Golden Delicious, Fuji, and Red Delicious), the peach, the pear and the kiwifruit all peaked at 675 nm, which was attributed to the absorption by chlorophyll in the fruit tissue. The kiwifruit had the highest chlorophyll absorption ($\mu_a = 1.1\ cm^{-1}$ at 675 nm), which could be expected from its greenish flesh. The white flesh peach had the lowest absorption value ($\mu_a = 0.3\ cm^{-1}$) at the chlorophyll absorption band among the five fruit samples (Fig. 7(a1)), which could be due to its low amount of chlorophyll content, as evidenced by its white-colored flesh. For the spectral range less than 550 nm, absorption due to carotenoid in the fruit tissue, which has an absorption peak at 480 nm (Merzlyak et al., 2003), became evident for the Golden Delicious and Fuji apples, the peach, the pear and the kiwifruit (Fig. 7 (a1)). For wavelengths between 730 and 900 nm, the absorption values of all the fruit and vegetable samples were relatively small and stable. Absorption values for these samples showed significant increases for wavelengths above 900 nm, and they peaked at 970 nm due to water absorption. Water has a weaker absorption around 760 nm. But this absorption peak was not observed on the absorption spectra presented in Fig. 7(a1) and (b1), which could be due to the fact that the current imaging system had a relatively low spectral resolution (4.54 nm) and hence it could not detect such small absorption peaks.

Absorption peaks due to chlorophyll absorption at 675 nm were not observed for the plum, cucumber, and zucchini squash samples (Fig. 7 (b1)). A strong absorption peak was found at 535 nm for the plum due to absorption by anthocyanin in the fruit tissue (Merzlyak et al., 2003), and at the same spectral position, a smaller absorption peak was also observed for the Red Delicious apple for the same reason. The cucumber and the zucchini squash showed similar patterns for their absorption spectra, which, however, were conspicuously different from those of other fruit samples. The μ_a spectra of these two vegetable samples were peaked at 550 and 720 nm, which were probably attributed to the absorption by turmeric and other pigments in the vegetable tissue.

Within the visible and short-wave near-infrared region, the values of μ_a for the fruit and vegetable samples in the relatively flat spectral range of 730–900 nm were generally lower, except for the Red Delicious apple, the cucumber and the zucchini squash, which had relatively large μ_a values in this spectra region. The maximum values of μ_a usually occurred at 675 and 535 nm, which corresponded to the absorption bands of major pigments (i.e., chlorophyll and anthocyanin).

Unlike the prominent 'fingerprints' appearing in the absorption spectra, the reduced scattering spectra of the fruit and vegetable samples did not show particular spectral features other than the trend of steadily decreasing μ_s' values with the increase of wavelength. Wavelength affects the number of multiple scattering interactions between photons and scattering particles in the samples. Generally, light has more scattering interactions in short wavelengths than in longer wavelengths, and hence the reduced scattering coefficient has larger values in short wavelengths than in longer wavelengths. Consequently, the minimum and maximum μ_s' values for the fruit and vegetable samples appeared at 1000 and 500 nm, respectively. The peach sample had the highest μ_s' values ($12.0–14.0\ cm^{-1}$) over the entire spectral region from 500 to 1000 nm, while μ_s' values were lower for the plum ($7.6–8.1\ cm^{-1}$). Other samples had intermediate values for the reduced scattering coefficient. Values of the parameters a and b in Eq. (8) were different for the μ_s' spectra of different fruits and vegetables, which suggested that the scattering particles in these samples may have different densities and average sizes. Hence, the reduced scattering coefficient could be potentially used to estimate quality attributes, such as firmness, of fruits and vegetables. It is worth noting that values of μ_s' were generally at least one order higher than those of μ_a for all the samples (except for the kiwifruit and plum around the wavelengths of 675 and 535 nm, respectively), indicating the dominant effect of scattering for photon transport in fruits and vegetables over the visible and short-wave near-infrared region.

Since large property variations exist among samples of the same type fruit or vegetable, values of the absorption and reduced scattering coefficients presented in Fig. 7 are not necessarily representative of these products. The overall patterns of the absorption and reduced scattering coefficients for the apple samples obtained using the spatially resolved steady-state hyperspectral imaging technique in this study are generally in agreement with those obtained by the method of time-resolved reflectance spectroscopy (Cubeddu et al., 2001a) and using a new spatial-frequency-domain technique (Anderson et al., 2007). Compared to the time-resolved method, the hyperspectral imaging technique covered a larger spectral region towards the short wavelengths (500–1000 nm), which included the absorption band of another important pigment (i.e., anthocyanin) in addition to chlorophyll. The hyperspectral imaging technique is noncontact, faster, less expensive, and easier for measuring turbid food and agricultural products. However, the measurement results from the spatially resolved hyperspectral imaging technique could be more influenced by the presence of sample skin or the surface layer, compared with the time-resolved technique. The optical properties obtained with the hyperspectral imaging technique reflect both surface (skin) and sub-surface layers (flesh) of tissue. It remains to be further investigated on the extent of the surface layer of horticultural products, to which it would affect the optical property measurement.

3.4. Application examples

Two application examples are given in this section of using optical properties to estimate the ripeness of tomatoes and light penetration depths for different fruits and vegetables.

3.4.1. Optical properties of tomatoes in relation to their ripeness

To demonstrate how optical properties may be used to assess fruit maturity and/or quality, we first examined spectra of the absorption coefficient of three tomatoes each with a different ripeness stage (green, pink, and red), which are shown in Fig. 8.

Dramatic changes in the pattern of the absorption spectra were observed for the tomatoes with different ripeness stages (Fig. 8(a)). The tomato with the green background color would contain a large amount of chlorophyll, and consequently it had a strong absorption peak at 675 nm. As a tomato fruit ripens from the green stage to the pink stage, its chlorophyll content decreases, while anthocyanin is produced and starts to increase. As a result, one would expect a trend of the decreasing absorption at 675 nm and increasing absorption at 535 nm from the green stage to the pink stage. This pattern of changes was clearly observed from the absorption spectra of the green and pink tomatoes shown in Fig. 8(a). When a tomato is fully ripe, chlorophyll would be greatly reduced or may disappear completely and anthocyanin becomes the dominant pigment in the fruit tissue. Consequently, one would expect a strong absorption peak at 535 nm for the red tomato due to the large amount of anthocyanin, along with the disappearance of the chlorophyll absorption at 675 nm. These are exactly what were observed from the absorption spectrum of the red tomato in Fig. 8(a). The green and red background colors are often related to the immature and mature conditions of tomatoes, respectively. Therefore, the μ_a values at 535 and 675 nm and/or their ratio could be used for evaluating the maturity or ripeness of tomatoes. Fig. 8(b) shows that all 60 tomatoes were correctly separated into three ripeness

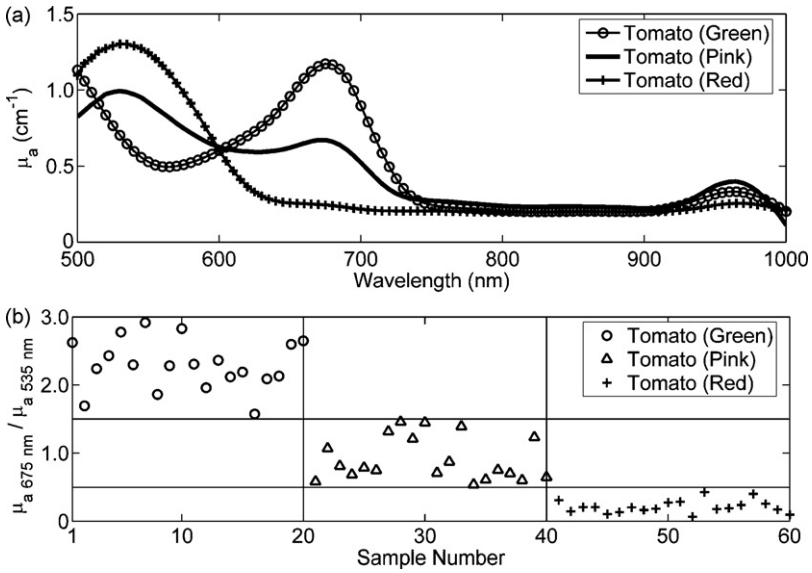

Fig. 8. (a) Absorption spectra of three tomatoes with green, pink, and red background colors and (b) the classification of 60 tomatoes into three ripeness groups (green, pink, and red) based on the ratio of the absorption coefficient at 675 nm to that at 535 nm.

stages based on the ratio of absorption values at 675 nm to those at 535 nm.

Considerable variations in the μ_s' spectra were also observed for the tomatoes with different levels of firmness (Fig. 9(a)). Hard tomatoes had consistently higher μ_s' values than the softer ones over the entire visible and short-wave near-infrared region. The softening process of tomatoes is accompanied with the weakening of cell walls and the disintegration of pectins binding the cell walls. Hence the density of the scattering particles in the fruit tissue would decrease during the softening process. The parameter a in Eq. (8) is proportional to the density of the scattering particles (Mourant et al., 1997), and it determines the absolute values of μ_s'. Thus soft tomatoes tended to have lower μ_s' values, whereas harder ones would be more conducive to the scattering of photons. This pattern of changes was clearly demonstrated in the μ_s' spectra for the tomatoes with three firmness levels (hard, medium, and soft) in Fig. 9(a). A simple correlation plot for the 60 tomatoes showed that the firmness of the tomatoes positively correlated with the value of μ_s' at each wavelength between 500 and 1000 nm (Fig. 9(b)). Correlations were greater than 0.50 at all wavelengths between 500 and 1000 nm, with the maximum r value of 0.66 at 790 nm. These results demonstrated that the reduced scattering coefficient could be useful for evaluating the firmness of tomatoes.

3.4.2. Estimated light penetration depths

With the knowledge of optical properties, we could estimate light penetration depths in the tested fruit and vegetable samples. Fig. 10 shows the estimated light penetration depths for one sample of each fruit and vegetable tested in this study. The minimum light penetration depths, ranging from 0.71 cm at 535 nm for the plum to 1.38 cm at 720 nm for the zucchini squash, generally occurred at the absorption peaks of the major pigments in the fruits and vegetables

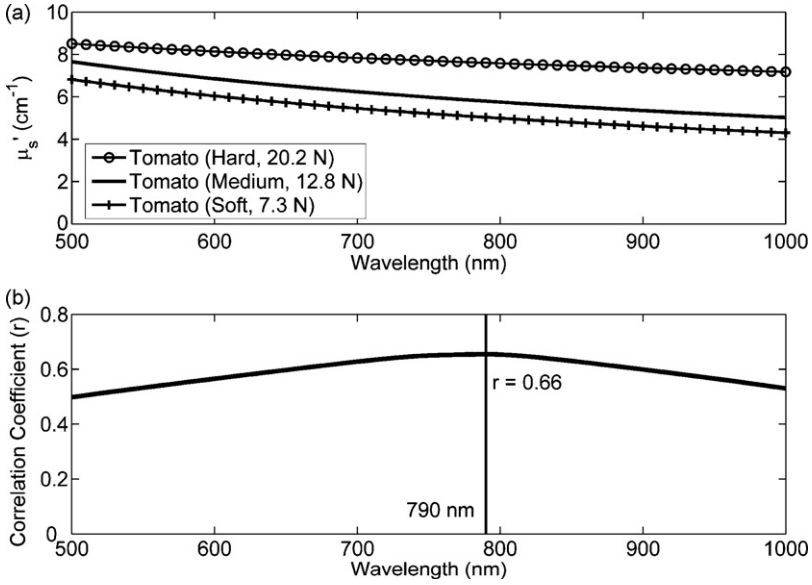

Fig. 9. (a) Spectra of the reduced scattering coefficient (μ_s') for three tomatoes at different firmness levels (hard, medium, and soft) and (b) a simple correlation plot between the measured Magness–Taylor fruit firmness and μ_s' over the wavelengths of 500–1000 nm.

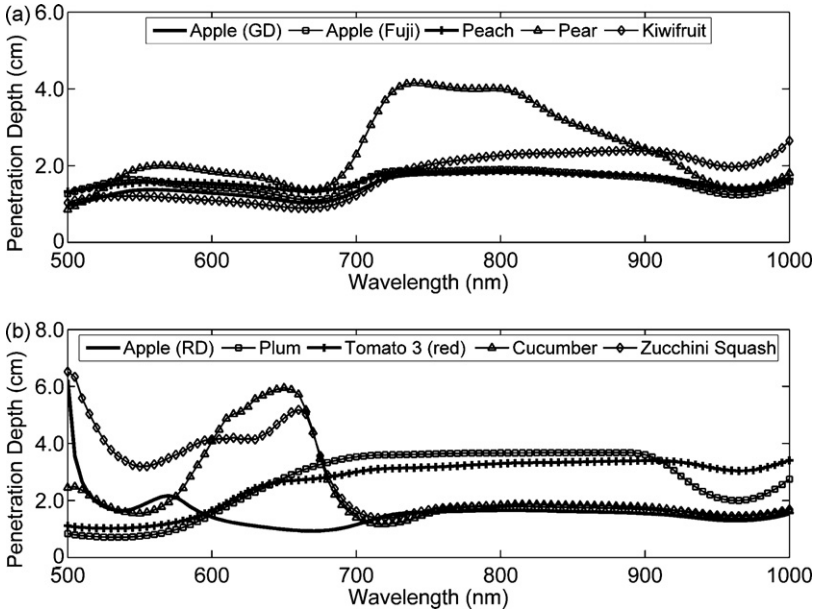

Fig. 10. Estimated light penetration depths for the fruit and vegetable samples (the symbols GD and RD represent 'Golden Delicious' and 'Red Delicious', respectively).

(535 nm for anthocyanin and 675 nm for chlorophyll). Penetration depths corresponding to the absorption bands of water at 970 nm and other minor pigments (e.g., anthocyanin in the Red Delicious apple at 535 nm) appeared as local minimums. Minimum penetration depths for the Golden Delicious apple, the peach and the pear were observed at 500 nm, where the μ_s' values were at the highest levels over the spectral region of 500–1000 nm and light absorption due to carotenoid in the fruit tissue exceeded the chlorophyll absorption (see Fig. 7(a1) and (a2)). On the other hand, the maximum penetration depths, ranging from 1.83 cm for the Golden Delicious apple to 6.52 cm for the zucchini squash, were located either in the flat absorption range of 730–900 nm (the Golden Delicious apple, the Fuji apple, the peach, the pear, and the plum) or at other spectral positions where the μ_a values reached their minimum levels (the kiwifruit, the Red Delicious apple, the cucumber, and the zucchini squash).

Light penetration depth is directly related to light attenuation in the fruit and vegetable tissues, which involves both absorption and scattering. Pigments and water are strong absorbing constituents in fruit and vegetable tissues, and they determine the major spectral features of light penetration in these products, although scattering properties are equally important for determining the absolute values of penetration depth (Eq. (7)). The overall patterns of light penetration depths in Golden Delicious and Fuji apples are consistent with those for Jonagold apples measured using an experimental method via an optical fiber probe (Lammertyn et al., 2000). The penetration depths estimated for these two varieties of apple in this study were larger than those for Jonagold apples (0.2–0.4 cm). Fraser et al. (2001) reported greater penetration depths, defined at a relative transmission intensity of 1% in the fruit tissue, than those in this study. Different results should have been expected since the definition of light penetration depth, instrument performance/setup, and fruit variety and condition were different in the current and other studies. Since large variations in the absorption and scattering properties exist among samples of the same type of fruit/vegetable, large differences in the estimated light penetration depths are also expected. Hence the estimated penetration depths presented in Fig. 10 may not represent typical values for these fruits and vegetables; instead, they show the general patterns that would be expected for these horticultural products. To establish the range of light penetration depths for a specific variety, a full-scale experiment with a large number of samples will be needed. Furthermore, the estimated light penetration depths are dependent on the measured optical properties, and the errors of light penetration estimations are directly proportional to the errors in the measured optical properties.

4. Concluding remarks

This research demonstrated that the spatially resolved steady-state hyperspectral imaging technique combined with inverse algorithms developed based on the diffusion theory model was useful for measuring the absorption and scattering properties of fresh fruits and vegetables over the spectral range of 500–1000 nm. The absorption spectra revealed major pigments (i.e., chlorophyll, anthocyanin, and carotenoid) in the tissues of the fruit and vegetable samples. The reduced scattering spectra steadily decreased towards the longer wavelengths with different values and slopes for different commodities. Significant absorption pattern changes were observed for tomatoes at different ripeness stages due to the changes of anthocyanin and chlorophyll content in the fruit tissue, and values of the reduced scattering coefficient decreased with the firmness of tomatoes. Strong absorbing constituents (i.e., pigments and water) in the fruit and vegetable tissues determined major spectral features of the light penetration depths. The two application examples demonstrated that optical properties could be useful for assessing fruit maturity/quality and estimating light penetration depths.

The spatially resolved hyperspectral imaging method is noncontact, relatively simple, and more suitable for horticultural products, compared to the time-resolved and frequency-domain methods. The method is, however, based on the diffusion theory model that is derived for homogeneous semi-infinite media, and thus it has limitations in application to horticultural products. Most horticultural products have a surface layer (skin) whose optical properties could be quite different from those of the sub-surface tissue. Hence the measurement results would inevitably reflect the properties of both the surface and sub-surface layers. For small size horticul-

tural product items, larger errors in the measured optical properties could be introduced due to their greater surface curvature. Further research is needed to better quantify these factors, so that the technique can be more effectively used for accurate measurement of the optical properties of horticultural and food products.

References

Anderson, E.R., Cuccia, D.J., Durkin, A.J., 2007. Detection of bruises on Golden Delicious apple using spatial-frequency-domain imaging. In: Proceedings of the SPIE, 6430, p. 64301O.

Chauchard, F., Roger, J.M., Bellon-Maurel, V., Abrahamsson, C., Andersson-Engels, S., Svanberg, S., 2005. MADSTRESS: a linear approach for evaluating scattering and absorption coefficients of samples measured using time-resolved spectroscopy in reflection. Appl. Spectrosc. 59, 1229–1235.

Cubeddu, R., D'Andrea, C., Pifferi, A., Taroni, P., Torricelli, A., Valentini, G., Dover, C., Johnson, D., Ruiz-Altisent, M., Valero, C., 2001a. Nondestructive quantification of chemical and physical properties of fruits by time-resolved reflectance spectroscopy in the wavelength range 650–1000 nm. Appl. Opt. 40, 538–543.

Cubeddu, R., D'Andrea, C., Pifferi, A., Taroni, P., Torricelli, A., Valentini, G., Ruiz-Altisent, M., Valero, C., Ortiz, C., Dover, C., Johnson, D., 2001b. Time-resolved reflectance spectroscopy applied to the nondestructive monitoring of the internal optical properties in apples. Appl. Spectrosc. 55, 1368–1374.

Dam, J.S., Pedersen, C.B., Dalgaard, T., Fabricius, P.E., Aruna, P., Andersson-Engels, S., 2001. Fiber-optic probe for noninvasive real-time determination of tissue optical properties at multiple wavelengths. Appl. Opt. 40, 1155–1164.

Doornbos, R.M.P., Lang, R., Aalders, M.C., Cross, F.W., Sterenborg, H.J.C.M., 1999. The determination of in vivo human tissue optical properties and absolute chromophore concentrations using spatially resolved steady-state diffuse reflectance spectroscopy. Phys. Med. Biol. 44, 967–981.

Farrell, T.J., Patterson, M.S., Wilson, B., 1992. A diffusion-theory model of spatially resolved steady-state diffuse reflectance for the noninvasive determination of tissue optical-properties in vivo. Med. Phys. 19, 879–888.

Fishkin, J.B., Coquoz, O., Anderson, E.R., Brenner, M., Tromberg, B.J., 1997. Frequency-domain photon migration measurements of normal and malignant tissue optical properties in a human subject. Appl. Opt. 36, 10–20.

Fraser, D.G., Kunnemeyer, R., McGlone, V.A., Jordan, R.B., 2001. Near infra-red (NIR) light penetration into an apple. Postharvest Biol. Technol. 22, 191–194.

Groenhuis, R.A.J., Ferwerda, H.A., Tenbosch, J.J., 1983a. Scattering and absorption of turbid materials determined from reflection measurements. 1. Theory. Appl. Opt. 22, 2456–2462.

Groenhuis, R.A.J., Tenbosch, J.J., Ferwerda, H.A., 1983b. Scattering and absorption of turbid materials determined from reflection measurements. 2. measuring method and calibration. Appl. Opt. 22, 2463–2467.

Kienle, A., Lilge, L., Patterson, M.S., Hibst, R., Steiner, R., Wilson, B.C., 1996. Spatially resolved absolute diffuse reflectance measurements for noninvasive determination of the optical scattering and absorption coefficients of biological tissue. Appl. Opt. 35, 2304–2314.

Kortüm, G., 1969. Reflectance Spectroscopy: Principles, Methods, Applications. Springer-Verlag, NY, USA.

Lammertyn, J., Peirs, A., De Baerdemaeker, J., Nicolai, B., 2000. Light penetration properties of NIR radiation in fruit with respect to non-destructive quality assessment. Postharvest Biol. Technol. 18, 121–132.

Lu, R., Chen, Y.R., 1998. Hyperspectral imaging for safety inspection of food and agricultural products. SPIE 3544, 121–133.

Lu, R., 2003. Imaging spectroscopy for assessing internal quality of apple fruit. ASAE Paper No. 036012. ASAE, St. Joseph, MI.

Lu, R., Peng, Y., 2006. Hyperspectral scattering for assessing peach fruit firmness. Biosyst. Eng. 93, 161–171.

Lu, R., 2007. Nondestructive measurement of firmness and soluble solids content for apple fruit using hyperspectral scattering images. Sens. Instrum. Food Qual. 1, 19–27.

Merzlyak, M.N., Solovchenko, A.E., Gitelson, A.A., 2003. Reflectance spectral features and non-destructive estimation of chlorophyll, carotenoid and anthocyanin content in apple fruit. Postharvest Biol. Technol. 27, 197–211.

Mourant, J.R., Fuselier, T., Boyer, J., Johnson, T.M., Bigio, I.J., 1997. Predictions and measurements of scattering and absorption over broad wavelength ranges in tissue phantoms. Appl. Opt. 36, 949–957.

Nichols, M.G., Hull, E.L., Foster, T.H., 1997. Design and testing of a white-light, steady-state diffuse reflectance spectrometer for determination of optical properties of highly scattering systems. Appl. Opt. 36, 93–104.

Ntziachristos, V., Chance, B., 2001. Accuracy limits in the determination of absolute optical properties using time-resolved NIR spectroscopy. Med. Phys. 28, 1115–1124.

Palmer, G.M., Zhu, C.F., Breslin, T.M., Xu, F.S., Gilchrist, K.W., Ramanujam, N., 2006. Monte Carlo-based inverse model for calculating tissue optical properties. Part II. Application to breast cancer diagnosis. Appl. Opt. 45, 1072–1078.

Patterson, M.S., Chance, B., Wilson, B.C., 1989. Time resolved reflectance and transmittance for the noninvasive measurement of tissue optical-properties. Appl. Opt. 28, 2331–2336.

Patterson, M.S., Moulton, J.D., Wilson, B.C., Berndt, K.W., Lakowicz, J.R., 1991. Frequency-domain reflectance for the determination of the scattering and absorption properties of tissue. Appl. Opt. 30, 4474–4476.

Pham, T.H., Eker, C., Durkin, A., Tromberg, B.J., Andersson-Engels, S., 2001. Quantifying the optical properties and chromophore concentrations of turbid media by chemometric analysis of hyperspectral diffuse reflectance data collected using a fourier interferometric imaging system. Appl. Spectrosc. 55, 1035–1045.

Qin, J., Lu, R., 2007. Measurement of the absorption and scattering properties of turbid liquid foods using hyperspectral imaging. Appl. Spectrosc. 61, 388–396.

Roggan, A., Friebel, M., Dorschel, K., Hahn, A., Muller, G., 1999. Optical properties of circulating human blood in the wavelength range 400–2500 nm. J. Biomed. Opt. 4, 36–46.

Tuchin, V., 2000. Tissue Optics: Ligh Scattering Methods and Instruments for Medical Diagnosis. SPIE Press, Bellingham, WA, USA.

Valero, C., Ruiz-Altisent, M., Cubeddu, R., Pifferi, A., Taroni, P., Torricelli, A., Valentini, G., Johnson, D., Dover, C., 2004. Selection models for the internal quality of fruit, based on time domain laser reflectance spectroscopy. Biosyst. Eng. 88, 313–323.

Vo-Dinh, T., 2003. Biomedical Photonics Handbook. CRC Press, LLC, Boca Raton, FL, USA.

Wang, L.H., Jacques, S.L., 1995. Use of a laser-beam with an oblique angle of incidence to measure the reduced scattering coefficient of a turbid medium. Appl. Opt. 34, 2362–2366.

Williams, P., Norris, K. (Eds.), 2001. Near-infrared Technology in the Agricultural and Food Industries, 2nd ed. AACC, St. Paul, MN, USA.

Wilson, B.C., Jacques, S.L., 1990. Optical reflectance and transmittance of tissues: principles and applications. IEEE J. Quant. Electron. 26, 2186–2199.

Xia, J., Berg, E.P., Lee, J.W., Yao, G., 2007. Characterizing beef muscles with optical scattering and absorption coefficients in VIS-NIR region. Meat Sci. 75, 78–83.

Zhang, R., Verkruysse, W., Choi, B., Viator, J.A., Jung, R., Svaasand, L.O., Aguilar, G., Nelson, J.S., 2005. Determination of human skin optical properties from spectrophotometric measurements based on optimization by genetic algorithms. J. Biomed. Opt. 10 (Art. No. 024030).

Zonios, G., Perelman, L.T., Backman, V.M., Manoharan, R., Fitzmaurice, M., Van Dam, J., Feld, M.S., 1999. Diffuse reflectance spectroscopy of human adenomatous colon polyps in vivo. Appl. Opt. 38, 6628–6637.